Article

Engineered P450 Atom-Transfer Radical Cyclases are Bifunctional Biocatalysts: Reaction Mechanism and Origin of Enantioselectivity

Yue Fu, Heyu Chen, Wenzhen Fu, Marc Garcia-Borràs,* Yang Yang,* and Peng Liu*

ACCESS | Metrics & More | Article Recommendations | Supporting Information

ABSTRACT: New-to-nature radical biocatalysis has recently emerged as a powerful strategy to tame fleeting open-shell intermediates for stereoselective transformations. In 2021, we introduced a novel metalloredox biocatalysis strategy that leverages the innate redox properties of the heme cofactor of P450 enzymes, furnishing new-to-nature atom-transfer radical cyclases (ATRCases) with excellent activity and stereoselectivity. Herein, we report a combined computational and experimental study to shed light on the mechanism and origins of enantioselectivity for this system. Molecular dynamics and quantum mechanics/molecular mechanics (QM/MM) calculations revealed an unexpected role of the key beneficial mutation I263Q. The glutamine residue serves as an essential hydrogen bond donor that engages with the carbonyl moiety of the substrate to promote bromine atom abstraction and enhance the enantioselectivity of radical cyclization.

Therefore, the evolved ATRCase is a bifunctional biocatalyst, wherein the heme cofactor enables atom-transfer radical biocatalysis, while the hydrogen bond donor residue further enhances the activity and enantioselectivity. Unlike many enzymatic stereocontrol rationales based on a rigid substrate binding model, our computations demonstrate a high degree of rotational flexibility of the allyl moiety in an enzyme−substrate complex and succeeding intermediates. Therefore, the enantioselectivity is controlled by the radical cyclization transition states rather than the substrate orientation in ground-state complexes in the preceding steps. During radical cyclization, anchoring effects of the Q263 residue and steric interactions with the heme cofactor concurrently control the π-facial selectivity, allowing for highly enantioselective C−C bond formation. Our computational findings are corroborated by experiments with ATRCase mutants generated from site-directed mutagenesis.
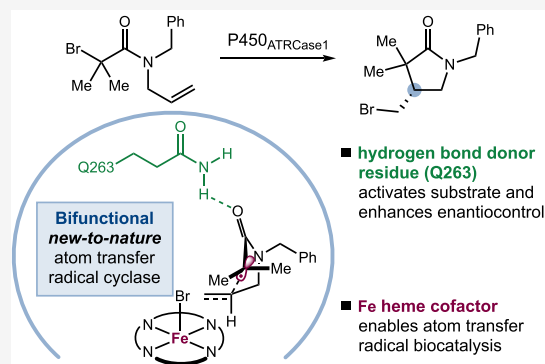
INTRODUCTION

Due to their ability to exert exquisite stereocontrol over challenging chemical reactions, enzymes are excellent catalysts for asymmetric synthesis in applications that range from small-scale synthesis to industrial manufacturing.[1] Traditional biocatalysis research focuses on the discovery, engineering, and application of naturally existing enzyme functions of outstanding synthetic value. However, compared to the immensely diverse range of organic reactions discovered and optimized by synthetic chemists, only a small subset of these reactivity patterns is found in natural enzymology and is currently being utilized by biocatalysis practitioners, thus imposing a major limitation on the utility of contemporary enzyme technologies. The implementation of unnatural chemistries by repurposing naturally existing enzymatic machineries promises to expand the reaction space of biocatalysis, thereby significantly augmenting the synthetic chemist's toolbox.[2]

Recently, we commenced a research program to repurpose naturally occurring metalloenzymes to catalyze unnatural stereoselective radical reactions using a metalloredox mechanism.[3] Almost 50% of naturally occurring proteins are metalloproteins,[4] among which redox-active first-row transi-

tion-metal cofactors such as Fe(II)/Fe(III),[5] Co(I)/Co(II),[6] and Cu(I)/Cu(II)[7] are ubiquitous. Cognizant of the tremendous synthetic potential of these metalloproteins in facilitating redox-mediated radical reactions, we recently repurposed cytochrome P450, a class of promiscuous metalloenzymes with numerous applications,[5a,b,8,9] to catalyze new-to-nature atom-transfer radical cyclization (ATRC) in an enantio- and diastereodivergent fashion (Figure 1a).[3] Due in large part to the difficulties in maintaining a tight association with the free-radical intermediate and/or the unfunctionalized olefin, inducing high levels of stereocontrol for free-radical-mediated olefin functionalization reactions continues to pose a formidable challenge for chiral small-molecule catalysts.[10] In particular, catalytic asymmetric ATRC reactions remain rare.[11] Thus, our evolved P450 atom-transfer radical cyclases provide
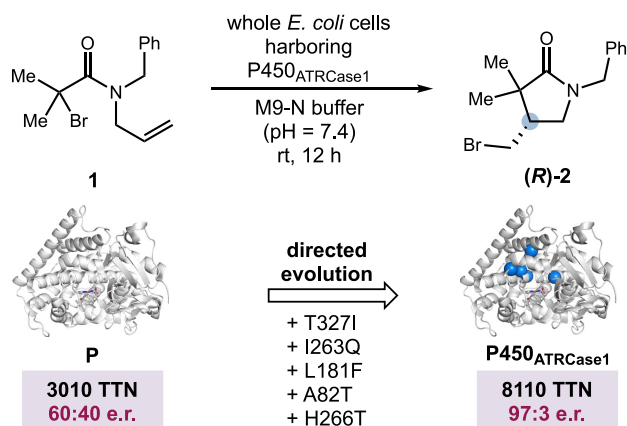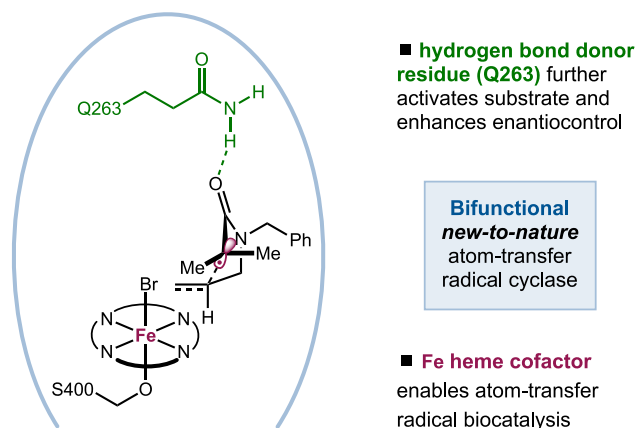
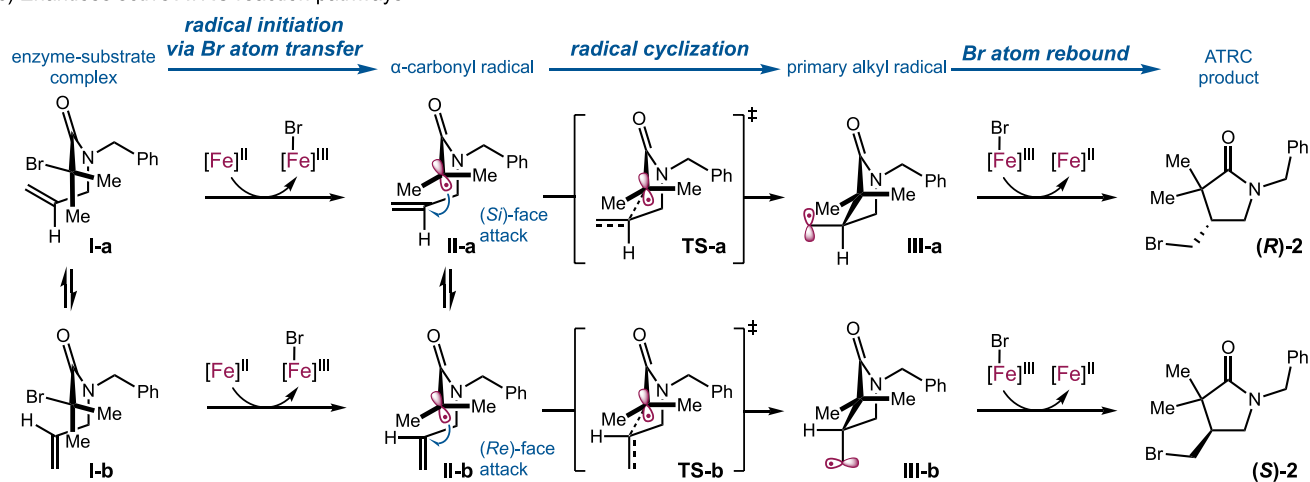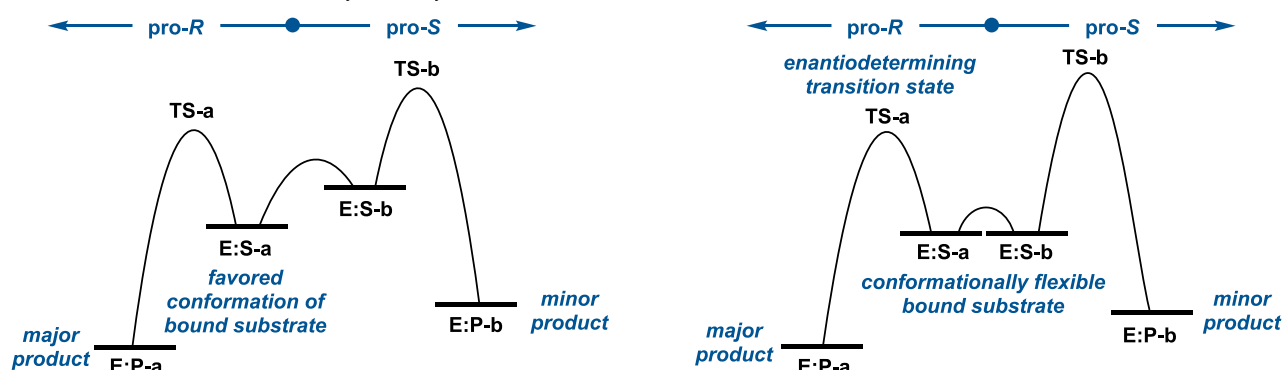**Figure 1.** P450-catalyzed enantioselective atom-transfer radical cyclization (ATRC).

a new means of taming radical intermediates for a synthetically valuable but underdeveloped class of asymmetric transformations. This metalloredox strategy is complementary to the elegant work of Hyster[12] and Zhao[13] on reductive C−C bond forming photoredox transformations using flavoenzymes, as the metallocofactor in our work allows redox-neutral atom-transfer reactions to proceed with excellent stereocontrol.

To further advance this recently developed mode of metalloredox radical biocatalysis, it is imperative to gain further understanding of the reaction mechanism and origin of enzyme-controlled stereoselectivity. The proposed mechanism

of this enzymatic ATRC reaction involves radical initiation via bromine atom-transfer from the substrate to the heme cofactor, enantioselective radical cyclization, and bromine atom rebound to form the product (Figure 1c). However, several key mechanistic questions remain unaddressed. First, our previous work showed that the evolved P450 radical cyclases displayed substantially faster kinetics and higher total turnover numbers relative to free cofactors in promoting this ATRC process,[3] but the origin of this enhanced activity is unclear. Second, the mode of enantioinduction for this radical-mediated olefin functionalization is potentially distinct from those of other

types of well-established natural and unnatural enzymatic reactions and remains to be uncovered. How these enhancements in reactivity and stereoselectivity related to key evolved structural elements of the ATRCase need to be elucidated.
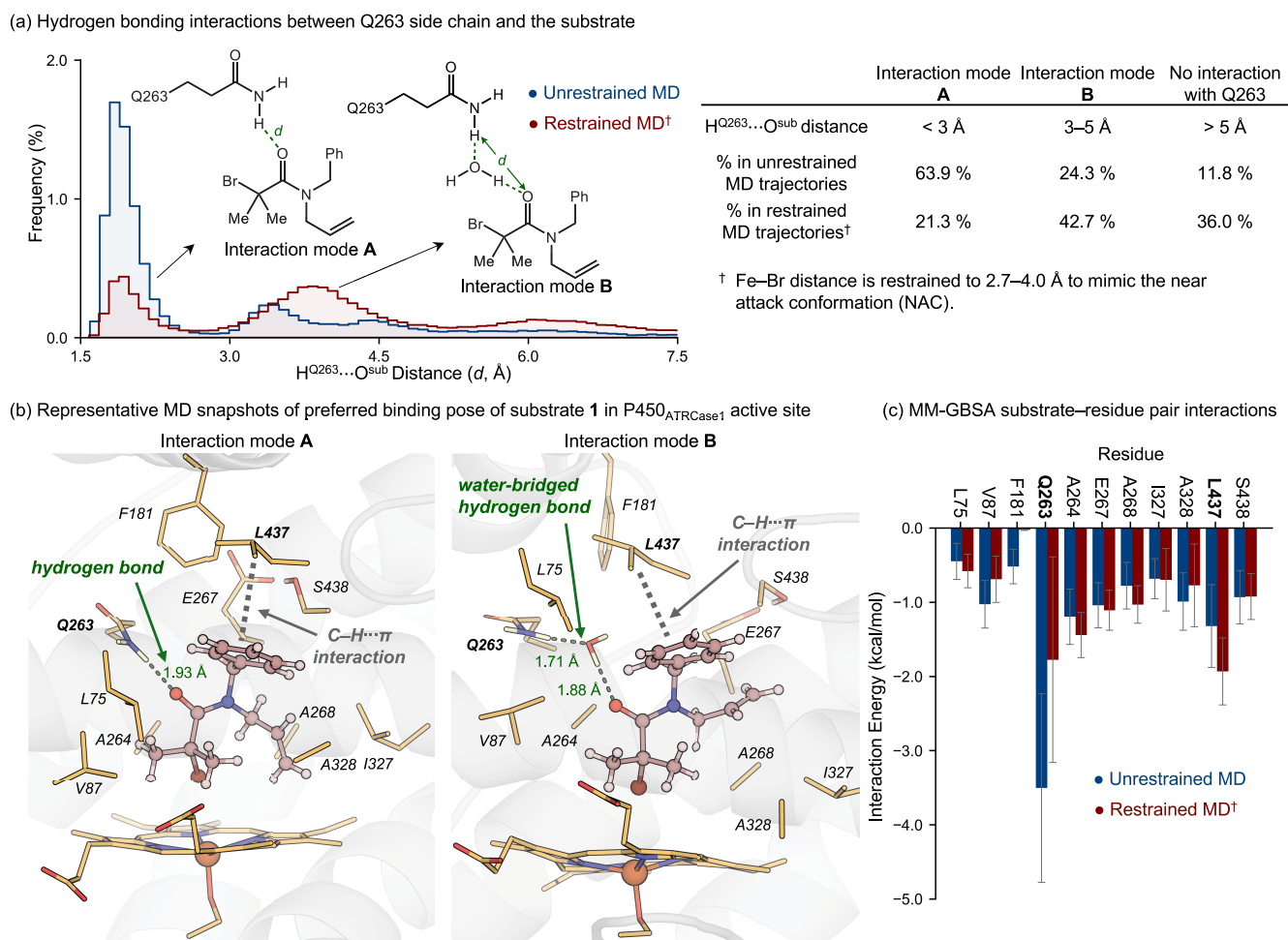
Stereocontrol of many enzymatic olefin functionalization reactions has been rationalized through π-facial selectivity models based on the ground-state structure of enzyme–substrate complexes,[13a,14] where the rotational freedom of the olefin is greatly reduced and the two prochiral π-faces are easily differentiated. Such intuitive substrate binding models obtained from experimental X-ray structures and computational substrate docking and/or classical molecular dynamics (MD) simulations have been widely used in biocatalysis and protein engineering. Nevertheless, an increasing number of studies underscored the importance of interrogating transition-state models to gain an accurate understanding of enzymatic stereoselectivities,[15,16] especially when the reactive functional group of the substrate (e.g., an olefin) does not strongly interact with the protein scaffold and is flexible in the enzyme–substrate complex (Figure 1d). In this situation, substrate binding models become ineffective, and computational models based on transition-state analysis are critical to describe the origin of enzymatic stereocontrol. In the recently developed biocatalytic enantioselective ATRC, it is not clear which enantioinduction scenario is operative. Depending on the conformational flexibility of the olefin moiety and the carbon-centered radical in the enzyme active site, the enantioselectivity may be rationalized by the substrate binding conformation or by the π-facial selectivity of the radical cyclization transition state (Figure 1d).

Herein, we performed computational studies to investigate the reaction mechanism and key factors promoting this new-to-nature atom-transfer radical cyclization and to explore the origin of enantioselectivity. We studied how interactions with active site residues facilitate the substrate activation step, leading to faster radical initiation. To compare the two enantioinduction scenarios (Figure 1d), we examined substrate binding modes and conformational flexibility of the olefin in the enzyme–substrate complex and the radical intermediate via classical MD simulations and hybrid quantum mechanics/molecular mechanics (QM/MM) metadynamics simulations. These ground-state behaviors are compared with transition-state enantiocontrol by computing the selectivity-determining radical cyclization transition states via QM/MM optimizations and QM/MM metadynamics[17] simulations. Our work revealed the highly flexible nature of the olefin in the enzyme–substrate complex, clearly demonstrating that enantiocontrol is governed by transition-state stability and not by the substrate conformational control upon binding. This study unveiled the unexpected role of a glutamine residue (Q263) acting as the hydrogen bond donor[13a,18] to activate the substrate toward radical initiation and enhance the enantioselectivity in radical cyclization (Figure 1b). The importance of this key residue in promoting reactivity and selectivity was then validated experimentally using enzyme variants derived from site-directed mutagenesis. Together, these studies showed that our directed evolution efforts led to the serendipitous discovery of a bifunctional biocatalyst, wherein the heme cofactor enables atom-transfer radical biocatalysis and the hydrogen bond donor residue further activates the substrate and enhances the enantioselectivity.

COMPUTATIONAL AND EXPERIMENTAL METHODS

Classical MD Simulations. In this study, we focused on the enzymatic reaction catalyzed by P450$_{ATRCase1}$, an (R)-product forming enzyme. The initial geometry of P450$_{ATRCase1}$ used in the modeling was generated by modifying the available X-ray crystal structure of a closely related P450 variant (PDB ID: 4H23).[19] Six mutations (A82T, L181F, I263Q, H266T, T327I, and T438S) were introduced into 4H23 using the mutagenesis tool in PyMOL[20] to prepare P450$_{ATRCase1}$. Classical molecular dynamics (MD) simulations were carried out using the pmemd module of the GPU-accelerated Amber 20 package.[21] Force field parameters for the iron–porphyrin complex were generated using the MCPB.py module[22] with the general Amber force field (GAFF).[23] Parameters for substrate **1** were generated using the GAFF force field, whereas the Amber ff14SB force field[24] was used for standard residues and TIP3P for solvent water molecules. First, three replicas[25] of independent 500 ns MD simulations were performed in the holo state of P450$_{ATRCase1}$ in the absence of substrate **1**. Clustering analysis based on the root-mean-square deviation (RMSD) of the protein backbone was carried out using the cpptraj module[26] to identify the most populated protein conformation in MD simulations of all three replicas. A representative snapshot of the most visited structure was used for docking calculations with substrate **1** using the AutoDock package.[27] Then, MD simulations of substrate-bound P450$_{ATRCase1}$ were performed with and without restraints to study the preferred substrate binding pose and the possible interaction modes between active site residues and the substrate. In the unrestrained MD simulations, three replicas of 500 ns simulations were performed without including external forces. In the restrained MD simulations, three replicas of 500 ns MD simulations were performed by restraining the Fe–Br distance (2.7–4.0 Å) by applying a harmonic potential of 500 kcal mol^{-1} Å^{-2}. These restraints were applied to simulate the substrate near attack conformation (NAC) in the inner-sphere bromine atom-transfer pathway. This strategy is similar to those applied in previous studies.[14c,28] The restrained distance range used (2.7–4.0 Å) was determined based on the Fe–Br distance observed in a density functional theory (DFT)-optimized dative complex using Fe–porphine as a model, which has a Fe–Br distance of 3.80 Å (see Figure S1 for details). Additional restrained classical MD simulations were performed by restraining both the Fe–Br distance and the hydrogen bond distance between the carbonyl group of the substrate and the amide of the Q263 residue (the H^{Q263}⋯O^{sub} distance was restrained in the range of 1–3 Å with a harmonic potential of 200 kcal mol^{-1} Å^{-2}). The most representative snapshots from the restrained MD simulations, based on protein backbone RMSD analysis, were used as the initial geometries for QM/MM calculations and QM/MM metadynamics simulations.

QM/MM Calculations of Reaction Energy Profiles. The ONIOM algorithm[29] implemented in Gaussian 16[30] was used in QM/MM calculations to characterize the stationary points (intermediates and transition states). Water molecules and counterions within 5 Å from the enzyme were included in the QM/MM calculations. Several conformers of the substrate were considered for each intermediate and transition state (see Figures S2 and S3 for higher energy conformers). The QM region includes the heme cofactor, the side chain of the Fe-binding serine residue (S400), the substrate, and boundary hydrogen atoms. This includes a total of 77 atoms in the QM region. For the QM region, the dispersion-corrected B3LYP[31]-D3[32]/6-31G(d)-LANL2DZ(Fe) level of theory was used in geometry optimization and vibrational frequency calculations, and the B3LYP-D3/6-311+G(d,p)-LANL2TZ(f)(Fe) level of theory was used in single-point energy calculations. This level of theory has been shown to provide good agreement with PNO-LCCSD(T)-F12 benchmark results.[3] For the MM region, the same force field parameters from the classical MD simulations discussed above were used. The quadratic coupled algorithm[33] and the mechanical embedding scheme were used in geometry optimization. Residues greater than 6 Å away from the QM region were kept fixed during geometry optimization. Single-point energy calculations were

(a) Hydrogen bonding interactions between Q263 side chain and the substrate

	Interaction mode A	Interaction mode B	No interaction with Q263
$H^{Q263}\cdots O^{sub}$ distance	< 3 Å	3–5 Å	> 5 Å
% in unrestrained MD trajectories	63.9 %	24.3 %	11.8 %
% in restrained MD trajectories[†]	21.3 %	42.7 %	36.0 %

[†] Fe–Br distance is restrained to 2.7–4.0 Å to mimic the near attack conformation (NAC).

(b) Representative MD snapshots of preferred binding pose of substrate **1** in P450$_{ATRCase1}$ active site

(c) MM-GBSA substrate–residue pair interactions

Figure 2. Classical MD simulations of the enzyme–substrate complex and analysis of substrate–protein interactions in the active site of P450$_{ATRCase1}$.

performed with the electronic embedding scheme, which better describes electrostatic interactions between QM and MM regions.[34] Open-shell singlet, triplet, quintet, and septet spin[35] states for each structure were considered. Wavefunction stability of all structures was confirmed using the "stable = opt" keyword.

QM/MM Metadynamics Simulations. All QM/MM Born Oppenheimer MD metadynamics simulations were performed with the CP2K 7.1 package,[36] combining the QM program QUICKSTEP[37] and the MM driver FIST. In this program, a real-space multigrid technique is used to compute the electrostatic coupling between the QM and MM regions.[38] The heme cofactor, the side chains of F181, Q263 (two key active site residues identified by protein engineering), and the Fe-binding S400, the substrate, and boundary hydrogen atoms were included in the QM region. This leads to 137 atoms in the QM region. The remaining part of the system was modeled at the MM level using the same parameters as in the classical MD simulations. The QM region was treated at the DFT (BLYP-D3) level,[39] employing the Gaussian and plane-wave method (GPW) that combines Gaussian-type basis functions and plane waves as an auxiliary basis. The DZVP basis set[40] and Goedecker–Teter–Hutter pseudopotentials[41] were employed. The auxiliary plane-wave basis set was expanded up to a 280 Ry cutoff. Trajectories starting from different initial geometries, obtained from snapshots of the restrained classical MD simulations, were simulated in the QM/MM metadynamics calculations. All QM/MM metadynamics simulations were performed in the NVT (constant number of atoms, volume, and temperature) ensemble using an integration time step of 0.5 fs. First, the system was equilibrated without any restraint for 2.0 ps. Then, the metadynamics method[17] was used to compute the free energy profiles.

In the simulations of the radical cyclization pathways, one collective variable was defined as the distance of the forming C–C bond between the radical center and the alkenyl carbon of the substrate. In the simulations to study the flexibility of the N-allyl group in the radical intermediate, two collective variables were defined as dihedral angles about the allylic C–C (ϕ) and N–C(allyl) (θ) bonds. Repulsive Gaussian-shaped potential hills with a height of 0.3 kcal/mol and a width of 0.1 bohr for distance and 0.1 rad for dihedral angle were added to the potential every 20 molecular dynamics steps.

Expression of P450$_{ATRCase1}$ Variants. *Escherichia coli* (E. coli BL21(DE3)) cells carrying plasmids encoding the indicated P450$_{ATRCase1}$ variant were grown overnight (12–14 h) in Luria broth with ampicillin (LBamp, 2.5 mL) in a culture tube. Preculture (1.5 mL, 5% v/v) was used to inoculate 30 mL of HBamp in a 125 mL Erlenmeyer flask. This culture was incubated at 37 °C, 230 rpm for 2 h in a New Brunswick Innova 44R shaker. The culture was then cooled on ice for 20 min and induced with 0.5 mM IPTG and 1.0 mM 5-aminolevulinic acid (final concentrations). Protein expression was conducted at 22 °C, 150 rpm, for 20–22 h. E. coli cells were then transferred to a 50 mL conical tube and pelleted by centrifugation (3000 rpm, 5 min, 4 °C) using an Eppendorf 5910R tabletop centrifuge. The supernatant was removed and the resulting cell pellet was resuspended in M9-N buffer to OD$_{600}$ = 30. An aliquot of this cell suspension (2 mL) was taken to determine the protein concentration by the hemochrome assay after cell lysis by sonication.

Biotransformations Using Whole E. coli Cells. Suspensions of E. coli cells expressing the P450$_{ATRCase1}$ variant in M9-N buffer (OD$_{600}$ = 30, pH = 7.40) were kept on ice. In another conical tube, a stock solution of D-glucose (500 mM in M9-N) was prepared. To a 2 mL
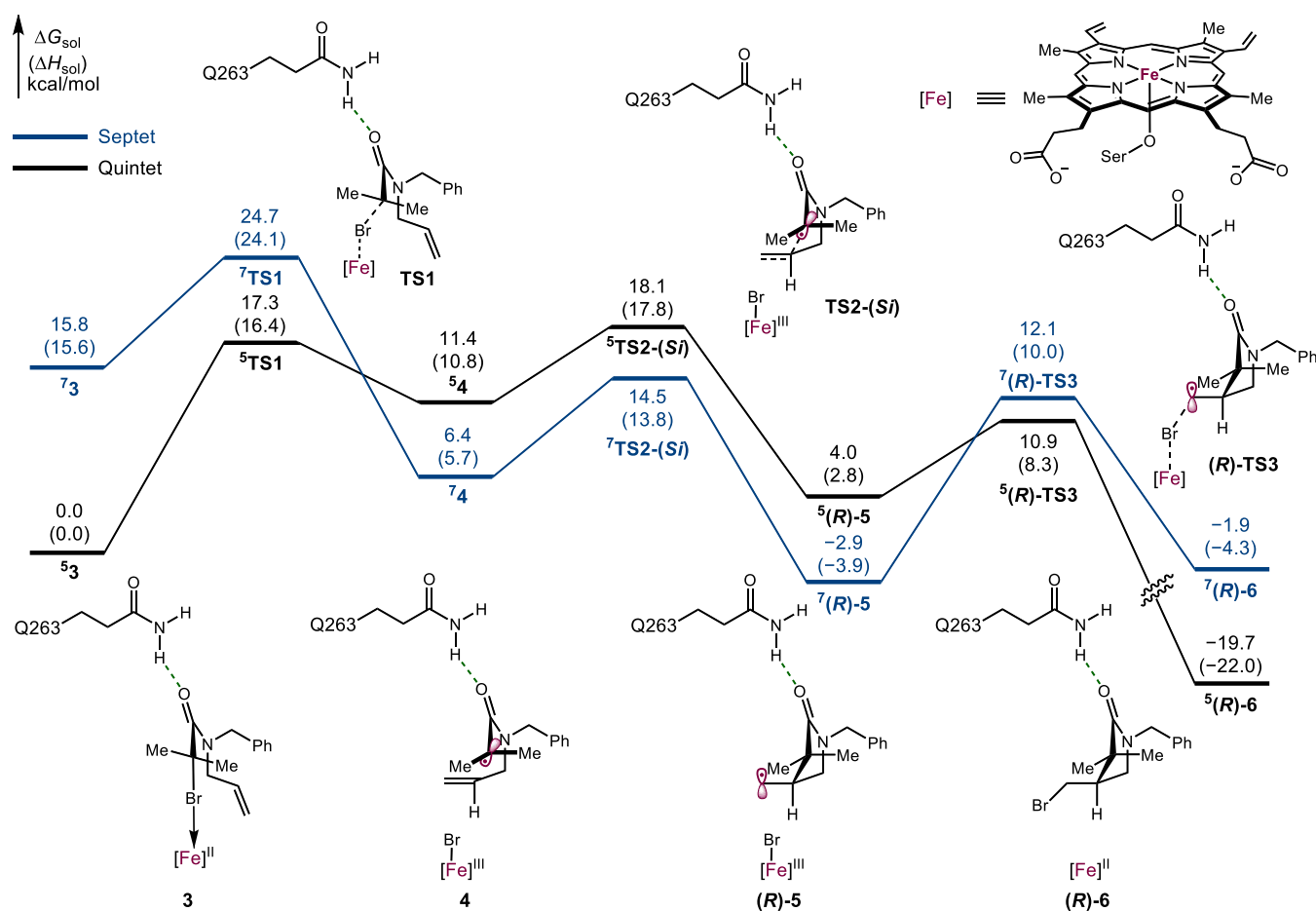
Figure 3. Computed Gibbs free energy profiles of the P450$_{ATRCase1}$-catalyzed ATRC from QM/MM calculations. The Gibbs free energies and enthalpies are with respect to a substrate–heme complex **3** where the bromine atom of the α-bromoamide substrate binds to the Fe center of the heme cofactor.

vial were added the suspension of *E. coli* cells (typically OD$_{600}$ = 30, 345 μL) and D-glucose (40 μL of 500 mM stock solution in M9-N buffer). This 2 mL vial was then transferred into an anaerobic chamber, where the ATRC substrate (15 μL of 270 mM stock solution in EtOH) was added. The final reaction volume was 400 μL; the final concentrations of the substrate and D-glucose were 10 and 50 mM, respectively. The vials were sealed and shaken in a Corning digital microplate shaker at room temperature and 680 rpm for 12 h. The reaction mixture was then extracted with 1:1 EtOAc/hexanes and analyzed by chiral high-performance liquid chromatography (HPLC) using mesitylene as the internal standard. For each P450$_{ATRCase1}$ variant, whole-cell reactions were performed in triplicate. Averaged yields and total turnover numbers (TTNs) were reported.
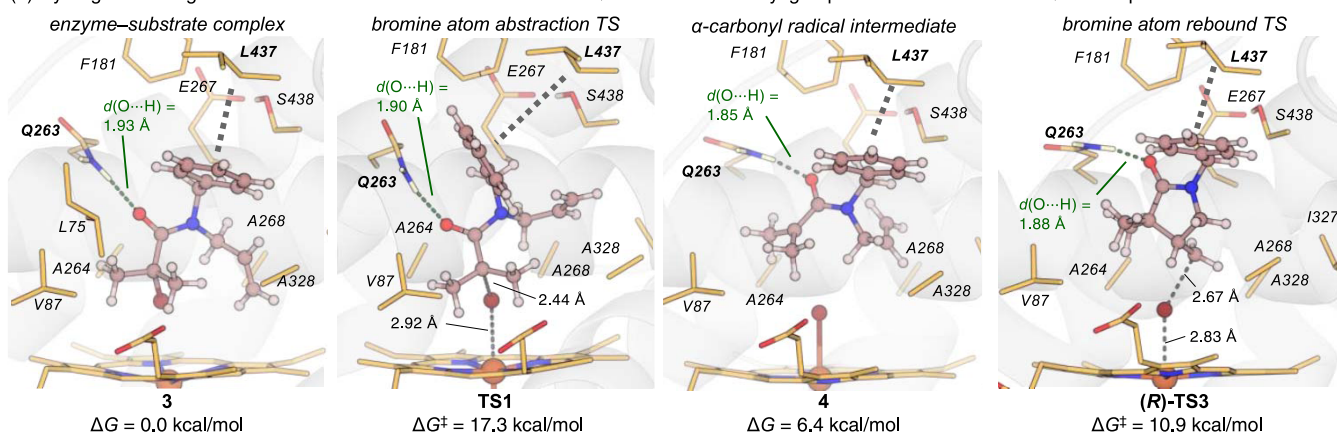
■ RESULTS AND DISCUSSION

Preferred Substrate Binding Pose and Unexpected Hydrogen Bonding Interaction with Key Residue Q263. To explore the preferred substrate binding pose and interaction modes between the substrate and active site residues, we performed classical MD simulations of the enzyme–substrate complex. After docking substrate **1** into the active site of P450$_{ATRCase1}$, we performed three replicas of 500 ns MD simulations without any restraint (unrestrained MD). We also performed another three replicas of 500 ns MD simulations by restraining the Fe–Br distance within 2.7–4.0 Å to mimic the near attack conformation (NAC)[14f,28] for bromine atom abstraction (restrained MD).
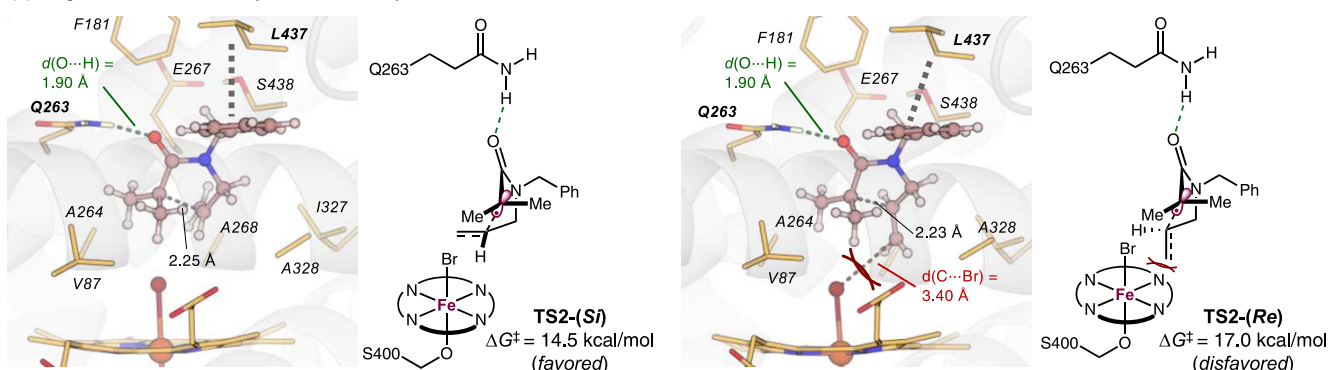
Both MD simulations revealed the existence of two dominant interaction modes with Q263 (Figure 2a), where the carbonyl group of the substrate forms a hydrogen bond with the NH$_2$ group of the side chain of Q263 (interaction mode **A**) or with a water molecule bridging Q263 and the substrate (interaction mode **B**). The unrestrained MD simulations revealed that in most of the simulation time (63.9%), the N–H⋯O distance between the side chain NH$_2$ group in Q263 and the amide carbonyl oxygen of **1** is shorter than 3 Å. In the restrained MD simulations, this direct Q263– substrate hydrogen bond was observed in a smaller percentage of the simulation time (21.2%) because the distance restriction between Fe and Br induces a less favorable spatial arrangement for the hydrogen bond. Nonetheless, most snapshots maintain a relatively short distance between Q263 and the substrate (<5 Å), with either a direct hydrogen bond with Q263's NH$_2$ group or a water-bridged hydrogen bond between these two groups (Figure 2a). These MD simulations suggest that hydrogen bonding interactions with Q263 are important for substrate binding and may be involved in subsequent steps of the catalytic cycle. This will be examined using QM/MM calculations in the next section.

Both unrestrained and restrained MD simulations describe a preferred binding pose of the substrate in which the *N*-benzyl group of **1** is placed in proximity to L437, establishing hydrophobic C–H⋯π interactions (Figure 2b). Due to this stabilizing interaction, the *s-cis* conformer of the amide is

(a) Hydrogen bonding interactions between the amide side chain of Q263 and the carbonyl group of substrate **1** in select QM/MM-optimized structures

enzyme–substrate complex

3
ΔG = 0.0 kcal/mol

bromine atom abstraction TS

TS1
ΔG‡ = 17.3 kcal/mol

α-carbonyl radical intermediate

4
ΔG = 6.4 kcal/mol

bromine atom rebound TS

(R)-TS3
ΔG‡ = 10.9 kcal/mol

(b) Origin of enantioselectivity in the radical cyclization transition states

TS2-(Si)
ΔG‡ = 14.5 kcal/mol
(favored)

TS2-(Re)
ΔG‡ = 17.0 kcal/mol
(disfavored)

Figure 4. QM/MM-optimized structures of select intermediates and transition states in the P450_ATRCase1-catalyzed ATRC of **1**. Gibbs free energies of all structures are with respect to **3**.

strongly favored within the active site, as seen in greater than 93% of the simulation time (see Figures S5 and S9 for details). In the favored *s-cis* conformer, the *N*-allyl group is *cis* to the bromoalkyl group, a conformation required in the subsequent radical cyclization step. In the absence of enzyme scaffold, rotation along the amide bond led to less efficient ATRC of *N*-allyl α-haloamides,[42] demonstrating the templating effect of the protein scaffold in facilitating radical catalysis. Overall, the preferred binding pose of **1** involves both hydrogen bonding interactions with the amide carbonyl and C−H···π interactions with the *N*-benzyl group. These interactions not only promote substrate binding but also stabilize the *s-cis* conformer of the amide poised to undergo radical cyclization. MM-GBSA substrate−residue pair interaction calculations[43] (Figure 2c) revealed that Q263 and L437 are among the residues establishing the most stabilizing interactions with the substrate, further highlighting their importance for substrate binding via hydrogen bonding and C−H···π interactions with these residues, respectively.

Reaction Energy Profiles from QM/MM Calculations and the Roles of Q263 on the Reactivity of Substrate Activation. We next used QM/MM methods to compute the free energy profile of this biocatalytic ATRC process. QM/MM calculations were performed starting from the preferred substrate binding pose characterized by MD simulations and considering the interaction mode **A** with Q263 residue (Figure 2b), where the amide side chain of Q263 engages the substrate in hydrogen bonding interactions. Open-shell singlet, triplet, quintet, and septet spin states of each intermediate and transition-state structure were optimized using QM/MM

(Figure S14). Gibbs free energy profiles involving the two most favorable spin states, quintet and septet, affording the major enantiomeric product (*R*)-**2** via radical addition to the (*Si*)-face of the alkene (**TS2-(Si)**) are shown in Figure 3. The quintet spin state was found to be the most favorable spin state for the enzyme−substrate and enzyme−product complexes and bromine atom abstraction and bromine atom rebound transition states (**TS1** and (**R**)-**TS3**), whereas the septet spin state was found to be the most stable in α-carbonyl radical **4**, radical cyclization transition state **TS2-(Si)**, and the succeeding cyclized primary radical (*R*)-**5** (see Figure S15 for spin densities of QM/MM-optimized structures).

The QM/MM-computed energy profiles revealed several key mechanistic features critical for the reactivity and enantioselectivity of this enzymatic ATRC. First, the Fe(II)/Fe(III) metalloredox processes (**TS1** and (**R**)-**TS3**) are both kinetically facile. Although the radical initiation via bromine atom abstraction (**TS1**) is endergonic by 6.4 kcal/mol, it requires a relatively low activation free energy of 17.3 kcal/mol. The endergonicity of this step is comparable to the bromine atom abstraction step in Cu-catalyzed atom-transfer radical polymerization (Cu-ATRP), which has an equilibrium constant of $K_{ATRP} = 10^{-9}$ to 10^{-4} in most common Cu-ATRP systems.[44] The relatively high HOMO energy of the heme cofactor (−3.3 eV, compared with −5.6 eV for Cu(TPMA)+, a representative Cu-ATRP catalyst)[45] suggests that this Fe-mediated bromine atom abstraction is kinetically promoted due to effective metal-to-substrate charge transfer in the bromine atom abstraction transition state.[46] Because bromine atom abstraction is the rate-determining step in the

F

QM/MM-computed catalytic cycle, a low kinetic barrier is essential for the reactivity of the ATRC. On the other hand, the exergonicity of the bromine atom rebound step enables rapid trapping of the enantioenriched cyclized primary radical intermediate (R)-**5** via (R)-**TS3**. Because the Gibbs free energy of (R)-**TS3** is lower than that of **TS2**-(Si), the radical cyclization (**TS2**-(Si)) is irreversible and thus determines the enantioselectivity.

The reactivity of bromine atom abstraction is promoted by hydrogen bonding interaction between the amide side chain in Q263 and the carbonyl group of substrate **1**. This hydrogen bond persists throughout catalysis among all of the QM/MM-optimized intermediate and transition-state structures (Figure 4). Furthermore, our QM/MM calculations showed slightly shorter N−H···O distances in bromine atom abstraction transition state **TS1** and α-carbonyl radical intermediate **4** compared to that in enzyme−substrate complex **3** (Figure 4a). These results indicate that this hydrogen bond not only promotes substrate binding but also more substantially stabilizes bromine atom abstraction TS and the radical being formed, promoting this rate-determining substrate activation step.[47] Further calculations using truncated model systems showed that this hydrogen bonding interaction lowers the energy of the lowest unoccupied molecular orbital (LUMO) orbital of the α-bromoamide moiety, thereby weakening the α-C−Br bond (see Figure S17 for the effects of hydrogen bonding interactions on LUMO energies and C−Br BDE).

The I263Q mutation represents one of the most important beneficial mutations in our previously reported directed evolution effort, as it led to dramatically enhanced activity and enantioselectivity of P450$_{ATRCase1}$. Compared to its parent, the I263Q mutant increased the total turnover number (TTN) from 1810 to 5370 and enantiomeric ratio (e.r.) from 67:33 to 89:11.[3] Despite these results, the role of this I263Q mutation was not known at the time P450$_{ATRCase1}$ was engineered. The computational results disclosed herein rationalized the role of Q263 on the experimentally observed reactivity. The higher e.r. with the I263Q variant suggests that this residue also plays a key role in the enantioselectivity-determining step. This effect is discussed in the next section.

Origin of Enantioselectivity and the Cooperative Effects of Q263 and Heme Cofactor on Enantioinduction. To understand the origin of enantioselectivity, we performed QM/MM calculations to study the enantioselectivity-determining radical cyclization transition states (Figure 4b). The transition state of radical addition to the (Si)-face of the alkenyl group **TS2**-(Si) leading to the experimentally observed major enantiomeric product (R)-**2** is 2.5 kcal/mol lower in energy than **TS2**-(Re) leading to the opposite enantiomeric product, (S)-**2**.

Hydrogen bonding interactions between Q263 and the carbonyl group of substrate **1** and C−H···π interactions between L437 and the N-benzyl group on **1** are observed in both optimized transition states **TS2**-(Si) and **TS2**-(Re) (Figure 4b). These interactions restrained the positioning of the substrate in the active site, placing the α-carbonyl radical center relatively close to the heme cofactor. When approaching the α-carbonyl radical during the radical cyclization, the alkenyl group is placed closer to the heme cofactor. In the favored radical cyclization transition state **TS2**-(Si), the alkenyl group points away from the heme, whereas in the disfavored transition state **TS2**-(Re), the alkenyl group points toward the heme, leading to unfavorable steric repulsions. This unfavor-

able steric effect is evidenced by the short distance between the terminal olefinic carbon and the bromine atom on heme (3.40 Å) in **TS2**-(Re).
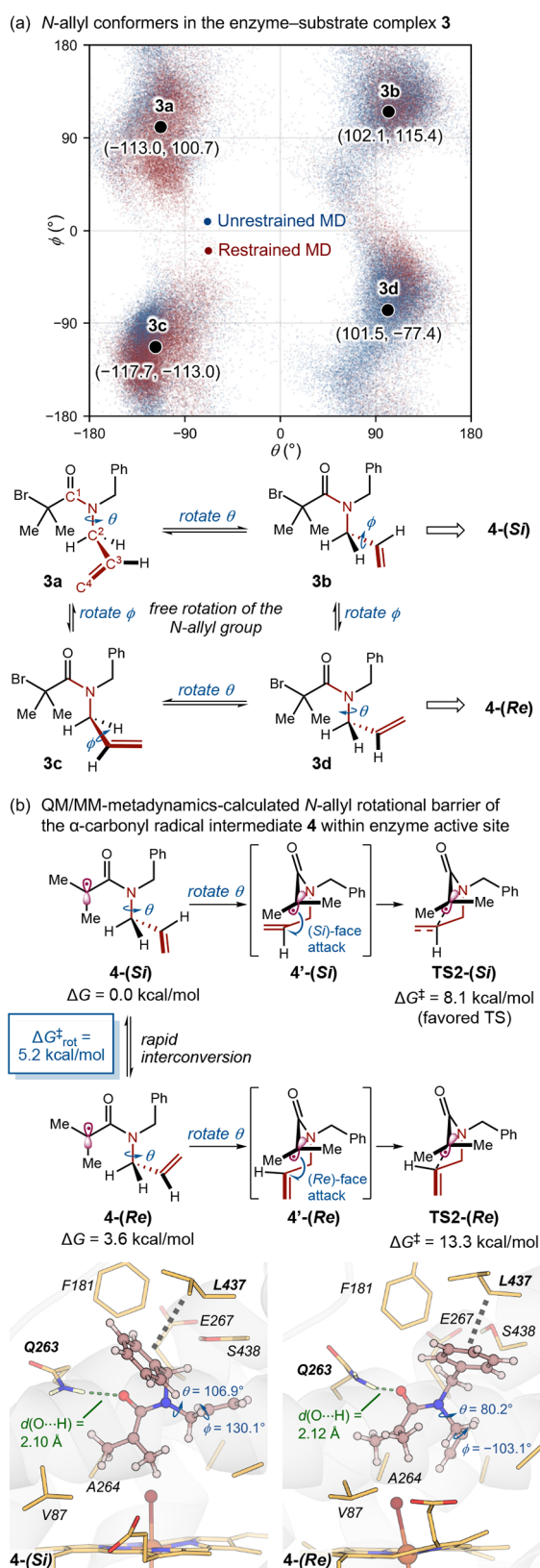
Next, we performed QM/MM metadynamics simulations to study the structural features along the radical cyclization reaction coordinate. The radical cyclization transition-state geometries and activation free energies characterized from QM/MM metadynamics are similar to those obtained from QM/MM geometry optimizations (see Figure S19 for details). The QM/MM metadynamics trajectories indicate that the Q263−substrate hydrogen bond along the radical cyclization pathway to form (R)-**2** via **TS2**-(Si) remains relatively strong with an average H^{Q263}···O^{sub} distance smaller than 2.5 Å (Figure 5).[48] On the other hand, the hydrogen bonding
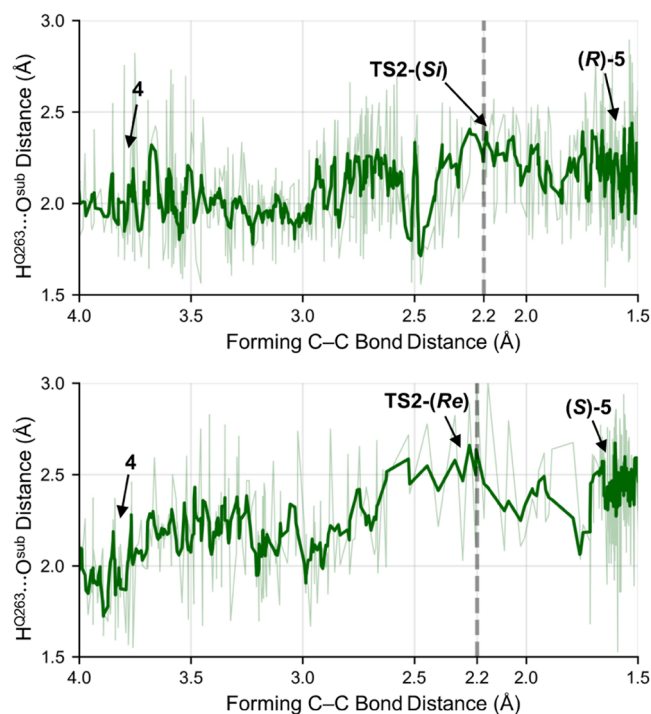
Figure 5. Q263 hydrogen bonding interactions along the radical cyclization pathways from QM/MM metadynamics simulations. The moving averages are shown in dark green lines.

interaction with Q263 is weaker in the region near the disfavored transition state **TS2**-(Re), evidenced by slightly longer H^{Q263}···O^{sub} distances explored along the disfavored radical cyclization pathway. The steric repulsions with heme lead to unfavorable distortion of **TS2**-(Re), weakening the hydrogen bond with Q263, a key enzyme−substrate interaction. Overall, both the QM/MM and the metadynamics simulations highlighted the cooperative effects of the Q263 residue, hydrophobic active site residues, such as L437, and the heme cofactor in anchoring the substrate and exerting steric interactions to affect the enantioinduction in radical cyclization transition states.

Classical MD and QM/MM Metadynamics Simulations on the Conformational Flexibility of the N-Allyl Group in Ground-State Complexes. We performed molecular dynamics simulations using both classical MD and QM/MM metadynamics to explore the conformational flexibility of the N-allyl group in enzyme−substrate complex **3** and α-carbonyl radical intermediate **4** (Figure 6). We surmised that these

Figure 6. Conformational change of the N-allyl group in enzyme–substrate complex **3** and α-carbonyl radical intermediate **4** from (a) classical MD and (b) QM/MM metadynamics simulations. The black dots in panel (a) indicate the centroids of each cluster representing the rotamers about the N−C(allyl) (θ) and allylic C−C (φ) bonds.

simulations, in conjunction with the transition-state modeling discussed above, would reveal which of the two enantioinduction scenarios shown in Figure 1d is operative in this enzymatic ATRC. In particular, these ground-state simulations could reveal whether the allyl group rotation is restricted prior to the radical cyclization transition state, therefore, offering a binding-based enantioinduction model for π-facial discrimination.

The conformations of the N-allyl group in enzyme–substrate complex **3** observed along the unrestrained and restrained classical MD simulations are described in Figure 6a. These MD simulations showed four clusters of conformers (**3a–3d**) with almost equal distributions, resulting from rotations about the N−C(allyl) (θ) and the allylic C−C (φ) bond. In the centroids of each cluster, the allyl group and the carbonyl are anticlinal (θ is within 90−150° or −90 to −150°) rather than having the synperiplanar conformation (θ = 30 to −30°) in the radical cyclization transition states (see Figures S20 and S21 for representative snapshots of these conformers). The lack of sterically bulky residues around the N-allyl group allows for the facile conformational change in the enzyme–substrate complex. Due to this conformational flexibility of the N-allyl group, there is no clear preference for the (**Re**)- or the (**Si**)-face of the C=C double bond to be exposed to the α-bromoamide moiety.

Next, we performed QM/MM metadynamics simulations on α-carbonyl radical intermediate **4** to investigate the rate of N-allyl group rotation once the radical is formed (Figure 6b). In these simulations, we used the dihedral angles about the allylic C−C (φ) and N−C(allyl) (θ) bonds as the collective variables. Similar to conformers **3a–3d**, the allyl group and the carbonyl are anti- or synclinal in all of the low-energy conformers of **4** (Figure S21). These conformers isomerize to synperiplanar conformation, such as in **4′-(Si)** and **4′-(Re)**, via rotation about the N−C(allyl) (θ) bond prior to the radical cyclization transition state. Although **4′-(Si)** and **4′-(Re)** are not minima on the free energy surface, the conformational change to these synperiplanar structures is kinetically facile (see Figure S21 in the SI for the complete rotational free energy surface of the N-allyl group in **4**). The QM/MM metadynamics calculations indicate conformer **4-(Si)**, which leads to the favored (**Si**)-face radical cyclization after N−C(allyl) (θ) bond rotation and radical addition, is 3.6 kcal/mol more stable than conformer **4-(Re)**, which leads to the less favorable radical cyclization with the (**Re**)-face of the olefin. Here, **4-(Re)** is destabilized by steric repulsions between the terminal alkenyl group and heme cofactor, similar to the steric effect that destabilizes **TS2-(Re)**. The low barrier to the interconversion between **4-(Si)** and **4-(Re)** via allylic C−C bond (φ) rotation ($\Delta G_{rot}^{\ddagger}$ = 5.2 kcal/mol) indicates that the N-allyl conformational change is much faster than the radical cyclization ($\Delta G^{\ddagger}$ = 8.1 kcal/mol via **TS2-(Si)**). The interconversion barrier between **4-(Si)** and **4-(Re)** is comparable to that of N-allylamide in the absence of the enzyme (see Figure S22 for details), indicating minimal interactions between the allyl group and active site residues in the α-carbonyl radical intermediate.

Overall, these simulations indicated a highly flexible N-allyl group in both the enzyme-bound substrate and the enzyme-bound α-carbonyl radical intermediate. Due to the rapid conformational interconversion of the N-allyl group in these ground-state complexes, the enantioselectivity of this new-to-nature enzymatic ATRC process is solely determined by the

radical cyclization transition state and not by the initial substrate conformation.
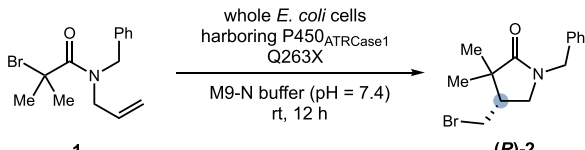
Experimental Investigations on the Importance of Residue 263 on Reactivity and Enantioselectivity. In light of the key role of residue Q263 uncovered by the computational studies, we generated P450$_{ATRCase1}$ Q263X mutants (X = R, K, N, S, A, I, and E) by site-directed mutagenesis and examined their catalytic activity and enantioselectivity in the radical cyclization of **1** (Table 1). In

Table 1. Experimental Validation[a]

entry	mutant	yield (%)[a]	TTN	e.r.[a]
1	none	89 ± 2	4400 ± 100	96:4
2	Q263R	82 ± 3	3700 ± 100	95:5
3	Q263K	76 ± 2	3730 ± 90	91:9
4	Q263N	75 ± 0	4340 ± 20	84:16
5	Q263S	36 ± 1	2310 ± 50	78:22
6	Q263A	37 ± 1	2490 ± 70	79:21
7	Q263I	52 ± 8	1300 ± 200	87:13
8	Q263E	25 ± 0	1300 ± 10	66:34

[a]Yields and e.r.'s were determined by HPLC analysis. Reactions were carried out using whole *E. coli* cells harboring P450$_{ATRCase1}$ mutants.

this study, other potential hydrogen bond donors, including arginine, lysine, asparagine, and serine, were evaluated in addition to residues lacking a hydrogen bond donor, including alanine, isoleucine, and glutamate.
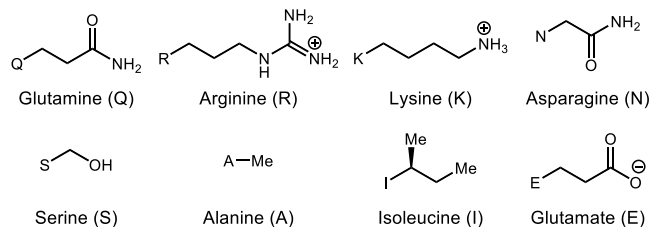
Consistent with our computational insights, when Q263 was replaced by an appropriate alternative hydrogen bond donor residue, similar enzyme activity and enantioselectivity were observed. The second-best residue at 263 was found to be arginine (R263, Table 1, entry 2), which bears a guanidine functional group that can potentially serve as a hydrogen bond donor. With this Q263R mutant, yield, total turnover number (TTN), and enantioselectivity very similar to the Q263 parent were observed. The Q263K mutant provided slightly further reduced enantioselectivity (entry 3). Interestingly, a further drop in e.r. was observed when this glutamine was replaced by an asparagine (entry 4), highlighting the importance of the tethering unit length for this hydrogen bond donor to engage the amide substrate. A263 lacking a hydrogen bond donor side chain and S263 with a much shorter hydrogen bond donor hydroxymethyl side chain provided greatly reduced enzyme activity and enantioselectivity (entries 5–6). Similar to the Q263A mutant, reverting this Q263 to I263 in native P450$_{BM3}$ led to inferior enzyme performance (entry 7). The E263 mutant bearing a presumably deprotonated glutamate at

residue 263 also provided low activity and enantioselectivity (entry 8). Together, these studies provided further evidence to support the essential role of residue Q263 of P450$_{ATRCase1}$, underscoring the importance of a hydrogen bond donor residue to both the enzyme activity and enantioselectivity.

CONCLUSIONS

Using a combined computational and experimental approach, we elucidated the mechanism and the origin of enantioselectivity of our recently developed biocatalytic atom-transfer radical cyclization using a laboratory-evolved P450 cyclase. QM/MM and classical MD simulations showed that the substrate binds to the enzyme active site, establishing stabilizing hydrogen bonding interactions with Q263 and C–H···π interactions with L437. While these stabilizing interactions are maintained throughout the catalytic process, leading to a relatively rigid positioning of the substrate carbonyl within the enzyme active site, the *N*-allyl group of the substrate is highly flexible and undergoes rapid conformational change in enzyme-bound forms. The facile conformational change of the *N*-allyl group in ground-state complexes makes the enantioselectivity entirely determined in the radical cyclization transition state. Notwithstanding the lack of conformational preference at the stage of various ground-state intermediates, high levels of enantioselectivity are achieved in the radical cyclization transition state where the olefin approaches the radical center, leading to further accentuated steric interactions with the heme cofactor. This study revealed the critical role of Q263 in promoting both reactivity and enantioselectivity, as it stabilizes substrate binding, promotes the rate-determining bromine atom abstraction, and controls the substrate orientation in the enantioselectivity-determining radical cyclization step. The multiple functions of Q263 were further corroborated by experiments evaluating the activity and enantioselectivity of enzyme variants generated by site-directed mutagenesis. Together, this study highlights the synergy between computations and experiments in providing insights into the mechanism of enantioinduction in radical-mediated enzymatic reactions. We expect that these insights will guide further engineering of stereoselective ATRCases and development of other asymmetric new-to-nature radical-mediated enzymatic reactions.

ASSOCIATED CONTENT

Ⓢ Supporting Information

The Supporting Information is available free of charge at https://pubs.acs.org/doi/10.1021/jacs.2c04937.

Additional computational results and experimental details (PDF)

AUTHOR INFORMATION

Corresponding Authors

Marc Garcia-Borràs − *Institut de Química Computacional i Catalisi (IQCC) and Departament de Química, Universitat de Girona, Girona 17003, Spain;* ⓞ orcid.org/0000-0001-9458-1114; Email: marc.garcia@udg.edu

Yang Yang − *Department of Chemistry and Biochemistry, University of California, Santa Barbara, California 93106, United States; Biomolecular Science and Engineering (BMSE) Program, University of California, Santa Barbara,*

California 93106, United States; ● orcid.org/0000-0002-4956-2034; Email: yang@chem.ucsb.edu

Peng Liu − *Department of Chemistry, University of Pittsburgh, Pittsburgh, Pennsylvania 15260, United States;* ● orcid.org/0000-0002-8188-632X; Email: pengliu@pitt.edu

Authors

Yue Fu − *Department of Chemistry, University of Pittsburgh, Pittsburgh, Pennsylvania 15260, United States;* ● orcid.org/0000-0003-3085-7817

Heyu Chen − *Department of Chemistry and Biochemistry, University of California, Santa Barbara, California 93106, United States;* ● orcid.org/0000-0002-6068-9386

Wenzhen Fu − *Department of Chemistry and Biochemistry, University of California, Santa Barbara, California 93106, United States;* ● orcid.org/0000-0002-8454-4720

Complete contact information is available at:
https://pubs.acs.org/10.1021/jacs.2c04937

Notes
The authors declare no competing financial interest.

■ ACKNOWLEDGMENTS

■ REFERENCES

(1) For reviews: (a) Reetz, M. T. Laboratory Evolution of Stereoselective Enzymes: A Prolific Source of Catalysts for Asymmetric Reactions. *Angew. Chem., Int. Ed.* **2011**, *50*, 138−174. (b) Bornscheuer, U. T.; Huisman, G. W.; Kazlauskas, R. J.; Lutz, S.; Moore, J. C.; Robins, K. Engineering the Third Wave of Biocatalysis. *Nature* **2012**, *485*, 185−194. (c) Devine, P. N.; Howard, R. M.; Kumar, R.; Thompson, M. P.; Truppo, M. D.; Turner, N. J. Extending the Application of Biocatalysis to Meet the Challenges of Drug Development. *Nat. Rev. Chem.* **2018**, *2*, 409−421. (d) Bornscheuer, U. T.; Hauer, B.; Jaeger, K. E.; Schwaneberg, U. Directed Evolution Empowered Redesign of Natural Proteins for the Sustainable Production of Chemicals and Pharmaceuticals. *Angew. Chem., Int. Ed.* **2019**, *58*, 36−40. (e) Zetzsche, L. E.; Chakrabarty, S.; Narayan, A. R. H. The Transformative Power of Biocatalysis in Convergent Synthesis. *J. Am. Chem. Soc.* **2022**, *144*, 5214−5225.
(2) For reviews: (a) Renata, H.; Wang, Z. J.; Arnold, F. H. Expanding the Enzyme Universe: Accessing Non-Natural Reactions by Mechanism-Guided Directed Evolution. *Angew. Chem., Int. Ed.* **2015**, *54*, 3351−3367. (b) Leveson-Gower, R. B.; Mayer, C.; Roelfes, G. The Importance of Catalytic Promiscuity for Enzyme Design and Evolution. *Nat. Rev. Chem.* **2019**, *3*, 687−705. (c) Chen, K.; Arnold, F. H. Engineering New Catalytic Activities in Enzymes. *Nat. Catal.* **2020**, *3*, 203−213. (d) Miller, D. C.; Athavale, S. V.; Arnold, F. H. Combining Chemistry and Protein Engineering for New-to-Nature

Biocatalysis. *Nat. Synth.* **2022**, *1*, 18−23. (e) Klaus, C.; Hammer, S. C. New Catalytic Reactions by Enzyme Engineering. *Trends Chem.* **2022**, *4*, 363−366.
(3) Zhou, Q.; Chin, M.; Fu, Y.; Liu, P.; Yang, Y. Stereodivergent Atom-Transfer Radical Cyclization by Engineered Cytochromes P450. *Science* **2021**, *374*, 1612−1616.
(4) Lu, Y.; Yeung, N.; Sieracki, N.; Marshall, N. M. Design of Functional Metalloproteins. *Nature* **2009**, *460*, 855−862.
(5) (a) Denisov, I. G.; Makris, T. M.; Sligar, S. G.; Schlichting, I. Structure and Chemistry of Cytochrome P450. *Chem. Rev.* **2005**, *105*, 2253−2278. (b) Shaik, S.; Kumar, D.; de Visser, S. P.; Altun, A.; Thiel, W. Theoretical Perspective on the Structure and Mechanism of Cytochrome P450 Enzymes. *Chem. Rev.* **2005**, *105*, 2279−2328. (c) Kovaleva, E. G.; Lipscomb, J. D. Versatility of Biological Non-Heme Fe(II) Centers in Oxygen Activation Reactions. *Nat. Chem. Biol.* **2008**, *4*, 186−193. (d) Poulos, T. L. Heme Enzyme Structure and Function. *Chem. Rev.* **2014**, *114*, 3919−3962.
(6) (a) Banerjee, R. Radical Carbon Skeleton Rearrangements: Catalysis by Coenzyme B12-Dependent Mutases. *Chem. Rev.* **2003**, *103*, 2083−2094. (b) Brown, K. L. Chemistry and Enzymology of Vitamin B12. *Chem. Rev.* **2005**, *105*, 2075−2150.
(7) Solomon, E. I.; Heppner, D. E.; Johnston, E. M.; Ginsbach, J. W.; Cirera, J.; Qayyum, M.; Kieber-Emmons, M. T.; Kjaergaard, C. H.; Hadt, R. G.; Tian, L. Copper Active Sites in Biology. *Chem. Rev.* **2014**, *114*, 3659−3853.
(8) Phillips, I. R.; Shephard, E. A.; de Montellano, P. R. O. *Cytochrome P450 Protocols*; Humana; Springer: Totowa, N.J., London, 2013.
(9) For reviews on new-to-nature carbene and nitrene transfer: (a) Brandenberg, O. F.; Fasan, R.; Arnold, F. H. Exploiting and Engineering Hemoproteins for Abiological Carbene and Nitrene Transfer Reactions. *Curr. Opin. Biotechnol.* **2017**, *47*, 102−111. (b) Yang, Y.; Arnold, F. H. Navigating the Unnatural Reaction Space: Directed Evolution of Heme Proteins for Selective Carbene and Nitrene Transfer. *Acc. Chem. Res.* **2021**, *54*, 1209−1225.
(10) For reviews: (a) Sibi, M. P.; Manyem, S.; Zimmerman, J. Enantioselective Radical Processes. *Chem. Rev.* **2003**, *103*, 3263−3296. (b) Proctor, R. S. J.; Colgan, A. C.; Phipps, R. J. Exploiting Attractive Non-Covalent Interactions for the Enantioselective Catalysis of Reactions Involving Radical Intermediates. *Nat. Chem.* **2020**, *12*, 990−1004. (c) Mondal, S.; Dumur, F.; Gigmes, D.; Sibi, M. P.; Bertrand, M. P.; Nechab, M. Enantioselective Radical Reactions Using Chiral Catalysts. *Chem. Rev.* **2022**, *122*, 5842−5976.
(11) (a) Yang, D.; Gu, S.; Yan, Y.-L.; Zhu, N.-Y.; Cheung, K.-K. Highly Enantioselective Atom-Transfer Radical Cyclization Reactions Catalyzed by Chiral Lewis Acids. *J. Am. Chem. Soc.* **2001**, *123*, 8612−8613. (b) Chen, B.; Fang, C.; Liu, P.; Ready, J. M. Rhodium-Catalyzed Enantioselective Radical Addition of CX4 Reagents to Olefins. *Angew. Chem., Int. Ed.* **2017**, *56*, 8780−8784.
(12) (a) Biegasiewicz, K. F.; Cooper, S. J.; Gao, X.; Oblinsky, D. G.; Kim, J. H.; Garfinkle, S. E.; Joyce, L. A.; Sandoval, B. A.; Scholes, G. D.; Hyster, T. K. Photoexcitation of Flavoenzymes Enables a Stereoselective Radical Cyclization. *Science* **2019**, *364*, 1166−1169. (b) Page, C. G.; Cooper, S. J.; Dehovitz, J. S.; Oblinsky, D. G.; Biegasiewicz, K. F.; Antropow, A. H.; Armbrust, K. W.; Ellis, J. M.; Hamann, L. G.; Horn, E. J.; Oberg, K. M.; Scholes, G. D.; Hyster, T. K. Quaternary Charge-Transfer Complex Enables Photoenzymatic Intermolecular Hydroalkylation of Olefins. *J. Am. Chem. Soc.* **2021**, *143*, 97−102. (c) Gao, X.; Turek-Herman, J. R.; Choi, Y. J.; Cohen, R. D.; Hyster, T. K. Photoenzymatic Synthesis of α-Tertiary Amines by Engineered Flavin-Dependent "Ene"-Reductases. *J. Am. Chem. Soc.* **2021**, *143*, 19643−19647. (d) Nicholls, B. T.; Qiao, T.; Hyster, T. K. A Photoenzyme for Challenging Lactam Radical Cyclizations *Synlett* **2022**, *33*, 1204−1208. (e) Nicholls, B. T.; Oblinsky, D. G.; Kurtoic, S. I.; Grosheva, D.; Ye, Y.; Scholes, G. D.; Hyster, T. K. Engineering a Non-Natural Photoenzyme for Improved Photon Efficiency**. *Angew. Chem., Int. Ed.* **2022**, *61*, No. e202113842. (f) For a review: Ye, Y.; Fu, H.; Hyster, T. K. Activation Modes in Biocatalytic Radical

Cyclization Reactions. *J. Ind. Microbiol. Biotechnol.* **2021**, *48*, No. kuab021.

(13) (a) Huang, X.; Wang, B.; Wang, Y.; Jiang, G.; Feng, J.; Zhao, H. Photoenzymatic Enantioselective Intermolecular Radical Hydroalkylation. *Nature* **2020**, *584*, 69−74. (b) For a review: Harrison, W.; Huang, X.; Zhao, H. Photobiocatalysis for Abiological Transformations. *Acc. Chem. Res.* **2022**, *55*, 1087−1096.

(14) (a) Su, H.; Ma, G.; Liu, Y. Theoretical Insights into the Mechanism and Stereoselectivity of Olefin Cyclopropanation Catalyzed by Two Engineered Cytochrome P450 Enzymes. *Inorg. Chem.* **2018**, *57*, 11738−11745. (b) Biler, M.; Crean, R. M.; Schweiger, A. K.; Kourist, R.; Kamerlin, S. C. L. Ground-State Destabilization by Active-Site Hydrophobicity Controls the Selectivity of a Cofactor-Free Decarboxylase. *J. Am. Chem. Soc.* **2020**, *142*, 20216−20231. (c) Nakano, Y.; Black, M. J.; Meichan, A. J.; Sandoval, B. A.; Chung, M. M.; Biegasiewicz, K. F.; Zhu, T.; Hyster, T. K. Photoenzymatic Hydrogenation of Heteroaromatic Olefins Using 'Ene'-Reductases with Photoredox Catalysts. *Angew. Chem., Int. Ed.* **2020**, *59*, 10484−10488. (d) Hall, M. Enzymatic Strategies for Asymmetric Synthesis. *RSC Chem. Biol.* **2021**, *2*, 958−989. (e) Coleman, T.; Kirk, A. M.; Chao, R. R.; Podgorski, M. N.; Harbort, J. S.; Churchman, L. R.; Bruning, J. B.; Bernhardt, P. V.; Harmer, J. R.; Krenske, E. H.; De Voss, J. J.; Bell, S. G. Understanding the Mechanistic Requirements for Efficient and Stereoselective Alkene Epoxidation by a Cytochrome P450 Enzyme. *ACS Catal.* **2021**, *11*, 1995−2010. (f) Gergel, S.; Soler, J.; Klein, A.; Schülke, K. H.; Hauer, B.; Garcia-Borràs, M.; Hammer, S. C. Directed Evolution of a Ketone Synthase for Efficient and Highly Selective Functionalization of Internal Alkenes by Accessing Reactive Carbocation Intermediates. Summitted 2022-01-05 *ChemRxiv* **2022**, DOI: 10.26434/chemrxiv-2022-dp94p. (accessed June 27, 2022).

(15) For reviews: (a) Sheng, X.; Kazemi, M.; Planas, F.; Himo, F. Modeling Enzymatic Enantioselectivity Using Quantum Chemical Methodology. *ACS Catal.* **2020**, *10*, 6430−6449. (b) Reetz, M. T.; Garcia-Borràs, M. The Unexplored Importance of Fleeting Chiral Intermediates in Enzyme-Catalyzed Reactions. *J. Am. Chem. Soc.* **2021**, *143*, 14939−14950.

(16) (a) Tang, W.; Jiménez-Osés, G.; Houk, K. N.; van der Donk, W. A. Substrate Control in Stereoselective Lanthionine Biosynthesis. *Nat. Chem.* **2015**, *7*, 57−64. (b) Bauer, P.; Carlsson, Å. J.; Amrein, B. A.; Dobritzsch, D.; Widersten, M.; Kamerlin, S. C. L. Conformational Diversity and Enantioconvergence in Potato Epoxide Hydrolase 1. *Org. Biomol. Chem.* **2016**, *14*, 5639−5651. (c) Sun, Z.; Wu, L.; Bocola, M.; Chan, H. C. S.; Lonsdale, R.; Kong, X.-D.; Yuan, S.; Zhou, J.; Reetz, M. T. Structural and Computational Insight into the Catalytic Mechanism of Limonene Epoxide Hydrolase Mutants in Stereoselective Transformations. *J. Am. Chem. Soc.* **2018**, *140*, 310−318. (d) Sato, M.; Kishimoto, S.; Yokoyama, M.; Jamieson, C. S.; Narita, K.; Maeda, N.; Hara, K.; Hashimoto, H.; Tsunematsu, Y.; Houk, K. N.; Tang, Y.; Watanabe, K. Catalytic Mechanism and Endo-to-Exo Selectivity Reversion of an Octalin-Forming Natural Diels−Alderase. *Nat. Catal.* **2021**, *4*, 223−232. (e) Dong, Y.; Li, T.; Zhang, S.; Sanchis, J.; Yin, H.; Ren, J.; Sheng, X.; Li, G.; Reetz, M. T. Biocatalytic Baeyer−Villiger Reactions: Uncovering the Source of Regioselectivity at Each Evolutionary Stage of a Mutant with Scrutiny of Fleeting Chiral Intermediates. *ACS Catal.* **2022**, *12*, 3669−3680.

(17) (a) Laio, A.; Parrinello, M. Escaping Free-Energy Minima. *Proc. Natl. Acad. Sci. U.S.A.* **2002**, *99*, 12562−12566. (b) Ensing, B.; De Vivo, M.; Liu, Z.; Moore, P.; Klein, M. L. Metadynamics as a Tool for Exploring Free Energy Landscapes of Chemical Reactions. *Acc. Chem. Res.* **2006**, *39*, 73−81. (c) Hutter, J.; Iannuzzi, M.; Schiffmann, F.; VandeVondele, J. Cp2k: Atomistic Simulations of Condensed Matter Systems. *Wiley Interdiscip. Rev.: Comput. Mol. Sci.* **2014**, *4*, 15−25. (d) Valsson, O.; Tiwary, P.; Parrinello, M. Enhancing Important Fluctuations: Rare Events and Metadynamics from a Conceptual Viewpoint. *Annu. Rev. Phys. Chem.* **2016**, *67*, 159−184. (e) Bussi, G.; Laio, A.; Tiwary, P. Metadynamics: A Unified Framework for Accelerating Rare Events and Sampling Thermodynamics and Kinetics. In *Handbook of Materials Modeling: Methods: Theory and Modeling*, Andreoni, W.; Yip, S., Eds.; Springer International Publishing: Cham, 2020; pp 565−595.

(18) For previous computational studies on the roles of active site hydrogen bonding interactions, see: (a) Herschlag, D.; Eckstein, F.; Cech, T. R. The Importance of Being Ribose at the Cleavage Site in the Tetrahymena Ribozyme Reaction. *Biochemistry* **1993**, *32*, 8312−8321. (b) Adalsteinsson, H.; Maulitz, A. H.; Bruice, T. C. Calculation of the Potential Energy Surface for Intermolecular Amide Hydrogen Bonds Using Semiempirical and Ab Initio Methods. *J. Am. Chem. Soc.* **1996**, *118*, 7689−7693. (c) Shan, S.-o.; Herschlag, D. The Change in Hydrogen Bond Strength Accompanying Charge Rearrangement: Implications for Enzymatic Catalysis. *Proc. Natl. Acad. Sci. U.S.A.* **1996**, *93*, 14474−14479. (d) Khade, R. L.; Zhang, Y. Catalytic and Biocatalytic Iron Porphyrin Carbene Formation: Effects of Binding Mode, Carbene Substituent, Porphyrin Substituent, and Protein Axial Ligand. *J. Am. Chem. Soc.* **2015**, *137*, 7560−7563. (e) Yang, Z.; Doubleday, C.; Houk, K. N. QM/MM Protocol for Direct Molecular Dynamics of Chemical Reactions in Solution: The Water-Accelerated Diels−Alder Reaction. *J. Chem. Theory Comput.* **2015**, *11*, 5606−5612. (f) Mehmood, R.; Qi, H. W.; Steeves, A. H.; Kulik, H. J. The Protein's Role in Substrate Positioning and Reactivity for Biosynthetic Enzyme Complexes: The Case of SyrB2/SyrB1. *ACS Catal.* **2019**, *9*, 4930−4943. (g) Vennelakanti, V.; Qi, H. W.; Mehmood, R.; Kulik, H. J. When Are Two Hydrogen Bonds Better than One? Accurate First-Principles Models Explain the Balance of Hydrogen Bond Donors and Acceptors Found in Proteins. *Chem. Sci.* **2021**, *12*, 1147−1162. (h) Liu, Z.; Calvó-Tusell, C.; Zhou, A. Z.; Chen, K.; Garcia-Borràs, M.; Arnold, F. H. Dual-Function Enzyme Catalysis for Enantioselective Carbon−Nitrogen Bond Formation. *Nat. Chem.* **2021**, *13*, 1166−1172.

(19) Coelho, P. S.; Wang, Z. J.; Ener, M. E.; Baril, S. A.; Kannan, A.; Arnold, F. H.; Brustad, E. M. A Serine-Substituted P450 Catalyzes Highly Efficient Carbene Transfer to Olefins in Vivo. *Nat. Chem. Biol.* **2013**, *9*, 485−487.

(20) *PyMOL Molecular Graphics System*, version 2.0; Schrödinger, LLC, 2017.

(21) Case, D. A.; Aktulga, H. M.; Belfon, K.; Ben-Shalom, I. Y.; Brozell, S. R.; Cerutti, D. S.; Cheatham, T. E.; Cisneros, G. A.; Cruzeiro, V. W. D.; Darden, T. A.; Duke, R. E.; Giambasu, G.; Gilson, M. K.; Gohlke, H.; Goetz, A. W.; Harris, R.; Izadi, S.; Izmailov, S. A.; Jin, C.; Kasavajhala, K.; Kaymak, M. C.; King, E.; Kovalenko, A.; Kurtzman, T.; Lee, T. S.; LeGrand, S.; Li, P.; Lin, C.; Liu, J.; Luchko, T.; Luo, R.; Machado, M.; Man, V.; Manathunga, M.; Merz, K. M.; Miao, Y.; Mikhailovskii, O.; Monard, G.; Nguyen, H.; O'Hearn, K. A.; Onufriev, A.; Pan, F.; Pantano, S.; Qi, R.; Rahnamoun, A.; Roe, D. R.; Roitberg, A.; Sagui, C.; Schott-Verdugo, S.; Shen, J.; Simmerling, C. L.; Skrynnikov, N. R.; Smith, J.; Swails, J.; Walker, R. C.; Wang, J.; Wei, H.; Wolf, R. M.; Wu, X.; Xue, Y.; York, D. M.; Zhao, S.; Kollman, P. A. *AMBER 2020*; University of California: San Francisco, 2020.

(22) Li, P.; Merz, K. M. MCPB.Py: A Python Based Metal Center Parameter Builder. *J. Chem. Inf. Model.* **2016**, *56*, 599−604.

(23) Wang, J.; Wolf, R. M.; Caldwell, J. W.; Kollman, P. A.; Case, D. A. Development and Testing of a General Amber Force Field. *J. Comput. Chem.* **2004**, *25*, 1157−1174.

(24) Maier, J. A.; Martinez, C.; Kasavajhala, K.; Wickstrom, L.; Hauser, K. E.; Simmerling, C. ff14SB: Improving the Accuracy of Protein Side Chain and Backbone Parameters from Ff99SB. *J. Chem. Theory Comput.* **2015**, *11*, 3696−3713.

(25) Knapp, B.; Ospina, L.; Deane, C. M. Avoiding False Positive Conclusions in Molecular Simulation: The Importance of Replicas. *J. Chem. Theory Comput.* **2018**, *14*, 6127−6138.

(26) Roe, D. R.; Cheatham, T. E. PTRAJ and CPPTRAJ: Software for Processing and Analysis of Molecular Dynamics Trajectory Data. *J. Chem. Theory Comput.* **2013**, *9*, 3084−3095.

(27) Morris, G. M.; Huey, R.; Lindstrom, W.; Sanner, M. F.; Belew, R. K.; Goodsell, D. S.; Olson, A. J. AutoDock4 and AutoDockTools4: Automated Docking with Selective Receptor Flexibility. *J. Comput. Chem.* **2009**, *30*, 2785−2791.

(28) (a) Knorrscheidt, A.; Soler, J.; Hünecke, N.; Püllmann, P.; Garcia-Borràs, M.; Weissenborn, M. J. Accessing Chemo- and Regioselective Benzylic and Aromatic Oxidations by Protein Engineering of an Unspecific Peroxygenase. *ACS Catal.* 2021, 11, 7327−7338. (b) Garcia-Borràs, M.; Kan, S. B. J.; Lewis, R. D.; Tang, A.; Jimenez-Osés, G.; Arnold, F. H.; Houk, K. N. Origin and Control of Chemoselectivity in Cytochrome c Catalyzed Carbene Transfer into Si−H and N−H Bonds. *J. Am. Chem. Soc.* 2021, 143, 7114−7123. (c) Soler, J.; Gergel, S.; Hammer, S.; Garcia-Borràs, M. Enzymatic Control Over Reactive Intermediates Enables Direct Oxidation of Alkenes to Carbonyls by a P450 Iron-Oxo Species. Summitted 2022-01-27 *ChemRxiv* DOI: 10.26434/chemrxiv-2022-6lpjf. (accessed June 27, 2022).

(29) Chung, L. W.; Sameera, W. M. C.; Ramozzi, R.; Page, A. J.; Hatanaka, M.; Petrova, G. P.; Harris, T. V.; Li, X.; Ke, Z.; Liu, F.; Li, H.-B.; Ding, L.; Morokuma, K. The ONIOM Method and Its Applications. *Chem. Rev.* 2015, 115, 5678−5796.

(30) Frisch, M. J.; Trucks, G. W.; Schlegel, H. B.; Scuseria, G. E.; Robb, M. A.; Cheeseman, J. R.; Scalmani, G.; Barone, V.; Petersson, G. A.; Nakatsuji, H.; Li, X.; Caricato, M.; Marenich, A. V.; Bloino, J.; Janesko, B. G.; Gomperts, R.; Mennucci, B.; Hratchian, H. P.; Ortiz, J. V.; Izmaylov, A. F.; Sonnenberg, J. L.; Williams-Young, D.; Ding, F.; Lipparini, F.; Egidi, F.; Goings, J.; Peng, B.; Petrone, A.; Henderson, T.; Ranasinghe, D.; Zakrzewski, V. G.; Gao, J.; Rega, N.; Zheng, G.; Liang, W.; Hada, M.; Ehara, M.; Toyota, K.; Fukuda, R.; Hasegawa, J.; Ishida, M.; Nakajima, T.; Honda, Y.; Kitao, O.; Nakai, H.; Vreven, T.; Throssell, K.; Montgomery, J. A.; Peralta, J. E.; Ogliaro, F.; Bearpark, M. J.; Heyd, J. J.; Brothers, E. N.; Kudin, K. N.; Staroverov, V. N.; Keith, T. A.; Kobayashi, R.; Normand, J.; Raghavachari, K.; Rendell, A. P.; Burant, J. C.; Iyengar, S. S.; Tomasi, J.; Cossi, M.; Millam, J. M.; Klene, M.; Adamo, C.; Cammi, R.; Ochterski, J. W.; Martin, R. L.; Morokuma, K.; Farkas, O.; Foresman, J. B.; Fox, D. J.. *Gaussian 16*, rev. C.01; Gaussian, Inc.: Wallingford, CT, 2016.

(31) (a) Lee, C.; Yang, W.; Parr, R. G. Development of the Colle-Salvetti Correlation-Energy Formula into a Functional of the Electron Density. *Phys. Rev. B* 1988, 37, 785−789. (b) Becke, A. D. Density-Functional Thermochemistry. III. The Role of Exact Exchange. *J. Chem. Phys.* 1993, 98, 5648−5652.

(32) Grimme, S. Semiempirical GGA-Type Density Functional Constructed with a Long-Range Dispersion Correction. *J. Comput. Chem.* 2006, 27, 1787−1799.

(33) Vreven, T.; Frisch, M. J.; Kudin, K. N.; Schlegel, H. B.; Morokuma, K. Geometry Optimization with QM/MM Methods II: Explicit Quadratic Coupling. *Mol. Phys.* 2006, 104, 701−714.

(34) Lin, H.; Truhlar, D. G. QM/MM: What Have We Learned, Where Are We, and Where Do We Go from Here? *Theor. Chem. Acc.* 2007, 117, No. 185.

(35) Araújo, J. Q.; de Mesquita Carneiro, J. W.; de Araujo, M. T.; Leite, F. H. A.; Taranto, A. G. Interaction between Artemisinin and Heme. A Density Functional Theory Study of Structures and Interaction Energies. *Bioorg. Med. Chem.* 2008, 16, 5021−5029.

(36) CP2K Open Source Molecular Dynamics, 2022. https://www.cp2k.org/quickstep. (accessed June 27, 2022).

(37) (a) Krack, M.; Parrinello, M. In *QUICKSTEP: Make the Atoms Dance; NIC Series*; Forschungszentrum Jülich, 2004; p 29. (b) VandeVondele, J.; Krack, M.; Mohamed, F.; Parrinello, M.; Chassaing, T.; Hutter, J. Quickstep: Fast and Accurate Density Functional Calculations Using a Mixed Gaussian and Plane Waves Approach. *Comput. Phys. Commun.* 2005, 167, 103−128.

(38) (a) Laio, A.; VandeVondele, J.; Rothlisberger, U. A Hamiltonian Electrostatic Coupling Scheme for Hybrid Car−Parrinello Molecular Dynamics Simulations. *J. Chem. Phys.* 2002, 116, 6941−6947. (b) Laino, T.; Mohamed, F.; Laio, A.; Parrinello, M. An Efficient Real Space Multigrid QM/MM Electrostatic Coupling. *J. Chem. Theory Comput.* 2005, 1, 1176−1184.

(39) (a) Becke, A. D. Density-Functional Exchange-Energy Approximation with Correct Asymptotic Behavior. *Phys. Rev. A* 1988, 38, 3098−3100. (b) Grimme, S.; Antony, J.; Ehrlich, S.; Krieg, H. A Consistent and Accurate ab initio Parametrization of Density Functional Dispersion Correction (DFT-D) for the 94 Elements H-Pu. *J. Chem. Phys.* 2010, 132, No. 154104.

(40) VandeVondele, J.; Hutter, J. Gaussian Basis Sets for Accurate Calculations on Molecular Systems in Gas and Condensed Phases. *J. Chem. Phys.* 2007, 127, No. 114105.

(41) Goedecker, S.; Teter, M.; Hutter, J. Separable Dual-Space Gaussian Pseudopotentials. *Phys. Rev. B* 1996, 54, 1703−1710.

(42) Curran, D. P.; Tamine, J. Effects of Temperature on Atom Transfer Cyclization Reactions of Allylic α-Iodo Esters and Amides. *J. Org. Chem.* 1991, 56, 2746−2750.

(43) (a) Miller, B. R.; McGee, T. D.; Swails, J. M.; Homeyer, N.; Gohlke, H.; Roitberg, A. E. MMPBSA.Py: An Efficient Program for End-State Free Energy Calculations. *J. Chem. Theory Comput.* 2012, 8, 3314−3321. (b) For a previous study using MM-GBSA calculations to analyze active site residue−substrate interactions, see: Ref 13.d.

(44) (a) Tang, W.; Kwak, Y.; Braunecker, W.; Tsarevsky, N. V.; Coote, M. L.; Matyjaszewski, K. Understanding Atom Transfer Radical Polymerization: Effect of Ligand and Initiator Structures on the Equilibrium Constants. *J. Am. Chem. Soc.* 2008, 130, 10702−10713. (b) Lin, C. Y.; Coote, M. L.; Gennaro, A.; Matyjaszewski, K. Ab Initio Evaluation of the Thermodynamic and Electrochemical Properties of Alkyl Halides and Radicals and Their Mechanistic Implications for Atom Transfer Radical Polymerization. *J. Am. Chem. Soc.* 2008, 130, 12762−12774.

(45) The HOMO energies of a model Fe−porphine complex and Cu(TMPA)$^+$ (TPMA: tris(2-pyridylmethyl)-amine) were computed at the B3LYP-D3/6-311+G(d,p)-LANL2TZ(f)/SMD(chlorobenzene)//B3LYP-D3/6-31G(d)-LANL2DZ level of theory. See Ref 3.

(46) For a computational study on the effects of HOMO energy of the transition metal complex on the rate of bromine atom abstraction, see: Fang, C.; Fantin, M.; Pan, X.; de Fiebre, K.; Coote, M. L.; Matyjaszewski, K.; Liu, P. Mechanistically Guided Predictive Models for Ligand and Initiator Effects in Copper-Catalyzed Atom Transfer Radical Polymerization (Cu-ATRP). *J. Am. Chem. Soc.* 2019, 141, 7486−7497.

(47) QM/MM calculations of an alternative bromine atom abstraction pathway without the hydrogen bond with Q263 predict a 1.9 kcal/mol higher barrier than that involving Q263 via **TS1**. See Figure S16 in the SI for details.

(48) The hydrogen bond distances in the metadynamics trajectories are longer than those in the QM/MM-optimized structures shown in Figure 4, because kinetic and potential energies were added to simulate the reaction at room temperature, whereas the QM/MM geometry optimizations obtain stationary points on the electronic energy surface.